J|A|C|S ARTICLES

Single Molecule Detection of Nitric Oxide Enabled by d(AT)₁₅ DNA Adsorbed to Near Infrared Fluorescent Single-Walled Carbon Nanotubes

Jingqing Zhang,[†,⊥] Ardemis A. Boghossian,[†,⊥] Paul W. Barone,[†] Alina Rwei,[†] Jong-Ho Kim,[†] Dahua Lin,[‡] Daniel A. Heller,[†] Andrew J. Hilmer,[†] Nitish Nair,[†,§] Nigel F. Reuel,[†] and Michael S. Strano*,[†]

Department of Chemical Engineering and Department of Electrical Engineering and Computer Science, Massachusetts Institute of Technology, Cambridge, Massachusetts 02139, United States

Received September 20, 2010; E-mail: strano@mit.edu

Abstract: We report the selective detection of single nitric oxide (NO) molecules using a specific DNA sequence of d(AT)₁₅ oligonucleotides, adsorbed to an array of near-infrared fluorescent semiconducting single-walled carbon nanotubes (AT₁₅−SWNT). While SWNT suspended with eight other variant DNA sequences show fluorescence quenching or enhancement from analytes such as dopamine, NADH, L-ascorbic acid, and riboflavin, d(AT)₁₅ imparts SWNT with a distinct selectivity toward NO. In contrast, the electrostatically neutral polyvinyl alcohol enables no response to nitric oxide, but exhibits fluorescent enhancement to other molecules in the tested library. For AT₁₅−SWNT, a stepwise fluorescence decrease is observed when the nanotubes are exposed to NO, reporting the dynamics of single-molecule NO adsorption via SWNT exciton quenching. We describe these quenching traces using a *birth-and-death* Markov model, and the maximum likelihood estimator of adsorption and desorption rates of NO is derived. Applying the method to simulated traces indicates that the resulting error in the estimated rate constants is less than 5% under our experimental conditions, allowing for calibration using a series of NO concentrations. As expected, the adsorption rate is found to be linearly proportional to NO concentration, and the intrinsic single-site NO adsorption rate constant is 0.001 s⁻¹ μM NO⁻¹. The ability to detect nitric oxide quantitatively at the single-molecule level may find applications in new cellular assays for the study of nitric oxide carcinogenesis and chemical signaling, as well as medical diagnostics for inflammation.

1. Introduction

Nitric oxide (NO) is an important cellular signaling molecule,[1−3] critical for maintaining vascular physiology[4−7] and regulating immune defense.[1,8] In addition, its paradoxical roles in carcinogenesis remain unclear, with experimental results that suggest both pro- and anticancer effects.[9−13] It has been established that there are two fundamental factors complicating the biological effects of NO in vivo: its concentration and its location of production.[9,11,13,14] Accurate detection of NO is essential to understanding its diverse biological roles. Difficulties arise mainly due to its rapid diffusivity and high reactivity with endogenous molecules, including oxygen, exposed thiols, other free radicals, and heme proteins.[15−21] In many cases, both the resultant short lifetime and its cellular reaction by products affect the accuracy of detection. Chemical approaches to the detection of nitric oxide or its reaction products have been a constant focus of research in recent years, most of which are on designing

---

[†] Department of Chemical Engineering.
[‡] Department of Electrical Engineering and Computer Science.
[§] Present address: Department of Chemical and Biological Engineering, University of Colorado at Boulder, Boulder, CO 80309.
[⊥] These authors contributed equally to this work.

(1) Moncada, S.; Palmer, R. M.; Higgs, E. A. *Pharmacol. Rev.* **1991**, *43*, 109.
(2) Garthwaite, J.; Boulton, C. L. *Annu. Rev. Physiol.* **1995**, *57*, 683.
(3) Steinert, J. R.; Chernova, T.; Forsythe, I. D. *Neuroscientist* **2010**, *16*, 435.
(4) Liu, V. W. T.; Huang, P. L. *Cardiovasc. Res.* **2008**, *77*, 19.
(5) Cai, H.; Harrison, D. G. *Circ. Res.* **2000**, *87*, 840.
(6) Gimbrone, M. A.; Topper, J. N.; Nagel, T.; Anderson, K. R.; Garcia-Cardena, G. In *Atherosclerosis V: The Fifth Saratoga Conference*; Numano, F., Gimbrone, M. A., Eds.; New York Academy of Sciences: New York, 2000; Vol. 902, p 230.
(7) Grange, R. W.; Isotani, E.; Lau, K. S.; Kamm, K. E.; Huang, P. L.; Stull, J. T. *Physiol. Genom.* **2001**, *5*, 35.
(8) Tripathi, P.; Kashyap, L.; Singh, V. *FEMS Immunol. Med. Microbiol.* **2007**, *51*, 443.
(9) Wink, D. A.; Mitchell, J. B. *Free Radic. Biol. Med.* **2003**, *34*, 951.
(10) Wink, D. A.; Vodovotz, Y.; Laval, J.; Laval, F.; Dewhirst, M. W.; Mitchell, J. B. *Carcinogenesis* **1998**, *19*, 711.

(11) Lancaster, J. R.; Xie, K. P. *Cancer Res.* **2006**, *66*, 6459.
(12) Hofseth, L. J.; Hussain, S. P.; Wogan, G. N.; Harris, C. C. *Free Radic. Biol. Med.* **2003**, *34*, 955.
(13) Hofseth, L. J. *Cancer Lett.* **2008**, *268*, 10.
(14) Rivot, J. P.; Barraud, J.; Montecot, C.; Jost, B.; Besson, J. M. *Brain Res.* **1997**, *773*, 66.
(15) Wink, D. A.; Mitchell, J. B. *Free Radic. Biol. Med.* **1998**, *25*, 434.
(16) Yao, D.; Vlessidis, A. G.; Evmiridis, N. P. *Microchim. Acta* **2004**, *147*, 1.
(17) Hetrick, E. M.; Schoenfisch, M. H. *Annu. Rev. Anal. Chem.* **2009**, *2*, 409.
(18) Williams, R. J. P. *Chem. Soc. Rev.* **1996**, *25*, 77.
(19) Moller, M. N.; Li, Q.; Lancaster, J. R.; Denicola, A. *IUBMB Life* **2007**, *59*, 243.
(20) Girard, P.; Potier, P. *FEBS Lett.* **1993**, *320*, 7.
(21) Thomas, D. D.; Ridnour, L. A.; Espey, M. G.; Donzelli, S.; Ambs, S.; Hussain, S. P.; Harris, C. C.; DeGraff, W.; Roberts, D. D.; Mitchell, J. B.; Wink, D. A. *J. Biol. Chem.* **2006**, *281*, 25984.

---

and synthesizing organic fluorophores[17,22−44] or quantum dots[45,46] that modulate fluorescence upon exposure to NO. Our laboratory has previously demonstrated that single-walled carbon nanotubes (SWNTs) wrapped in a diaminophenyl dextran are capable of detecting NO within live murine macrophages.[47] In the present work, we develop an alternate construct based on a specific DNA oligonucleotide that allows selective detection of NO at the single molecule level for the first time. This forms a basis for studying NO generation in cellular signaling networks, as we have previously demonstrated for the case of H_2O_2 signaling initiated by epidermal growth factor receptor (EGFR).[48,49]

The most extensively used method of NO quantification, the Griess assay, is robust but indirect, as it only measures the oxidation product of NO, or NO_2^-. Alternatively, NO-selective electrodes, electron paramagnetic resonance, and chemiluminescence assays may quantify NO directly with high sensitivity but often lack spatial resolution.[16,17,23] Fluorescence-based probes combined with microscopy are particularly useful for resolving spatial and temporal aspects of NO production.[17,22−24] Many techniques rely on the reaction of diamino-aromatics with either N_2O_3[25,26] or NO^+,[27−30] leading to the formation of a highly fluorescent product. A promising recent approach uses a 5-amino-1-naphthonitrile derivative with NO^+ to form a diazo ring that fluoresces in the red.[31] Although lacking direct reactivity with NO, these methods represent the state-of-the-art and are widely applied.[22] In addition, recent work on fluorescent nitric oxide cheletropic traps (FNOCT),[32,33] and metal-based probes[34−44] that react directly with NO, are also promising approaches. Organic fluorophores are highly sensitive and robust but also tend to photobleach, limiting their useful lifetime and often preventing quantitative analysis.[50]

SWNTs are used ubiquitously as chemical sensors of various types, with fluorescent sensing emerging as a particularly advantageous modality. SWNTs are cylindrical graphene layers with nanometer-sized diameters that emit stable near-infrared (NIR) light with no reported photobleaching threshold,[50−52] which allows for prolonged imaging in living cells and tissues.[47,50,53−55] Moreover, their one-dimensional electronic structure results in great sensitivity to analytes of interest. Previous work in our laboratory has demonstrated that a synthesized diaminophenyl-functionalized dextran polymer enables rapid and direct response of SWNT to NO.[47] Recently, single-molecule adsorption on the SWNT sidewall has been resolved through quenching of excitons,[48,49,56−59] enabling a new generation of optical sensors capable of the ultimate detection limit: single molecules. The recorded fluorescence modulation, supplemented with proper calibration, provides a means for evaluating the concentration of the quencher molecule, even at low concentrations.[47−49,55] Furthermore, compared with small molecule fluorescent probes, nondiffusive SWNTs allow otherwise impossible quantification of molecules with precise spatial resolution at the nanometer scale. This type of platform has recently demonstrated its capability by studying reactive oxygen species signaling at the single cell level.[49]

Here we report the first fluorescence-based SWNT sensing array made of single-stranded $d(AT)_{15}$ DNA oligonucleotide-wrapped SWNTs (AT_{15}−SWNT). This 30-base oligomer imparts SWNTs with the capability of directly, and selectively, quantifying NO concentrations. We find that the AT_{15}−SWNT complex is unique in its high selectivity toward NO when compared with a library of other DNA sequences and polymers. Each single AT_{15}−SWNT on the array exhibits an intense fluorescence signal at near-infrared wavelengths (900−1400 nm) and records the dynamics of single molecule NO adsorption and desorption on the SWNT through a quantized change in intensity. We develop a generic algorithm based on a *birth-and-death* Markov process to determine the local NO concentra-

(22) Gomes, A.; Fernandes, E.; Lima, J. *J. Fluoresc.* **2006**, *16*, 119.

(23) Nagano, T.; Yoshimura, T. *Chem. Rev.* **2002**, *102*, 1235.

(24) Miller, E. W.; Chang, C. J. *Curr. Opin. Chem. Biol.* **2007**, *11*, 620.

(25) Nagano, T. *Luminescence* **1999**, *14*, 283.

(26) Tarpey, M. M.; Wink, D. A.; Grisham, M. B. *Am. J. Physiol.* **2004**, *286*, R431.

(27) Kojima, H.; Sakurai, K.; Kikuchi, K.; Kawahara, S.; Kirino, Y.; Nagoshi, H.; Hirata, Y.; Nagano, T. *Chem. Pharm. Bull.* **1998**, *46*, 373.

(28) Kojima, H.; Nakatsubo, N.; Kikuchi, K.; Kawahara, S.; Kirino, Y.; Nagoshi, H.; Hirata, Y.; Nagano, T. *Anal. Chem.* **1998**, *70*, 2446.

(29) Kojima, H.; Urano, Y.; Kikuchi, K.; Higuchi, T.; Hirata, Y.; Nagano, T. *Angew. Chem., Int. Ed.* **1999**, *38*, 3209.

(30) Sasaki, E.; Kojima, H.; Nishimatsu, H.; Urano, Y.; Kikuchi, K.; Hirata, Y.; Nagano, T. *J. Am. Chem. Soc.* **2005**, *127*, 3684.

(31) Yang, Y.; Seidlits, S. K.; Adams, M. M.; Lynch, V. M.; Schmidt, C. E.; Anslyn, E. V.; Shear, J. B. *J. Am. Chem. Soc.* **2010**, *132*, 13114.

(32) Meineke, P.; Rauen, U.; de Groot, H.; Korth, H. G.; Sustmann, R. *Chem.—Eur. J.* **1999**, *5*, 1738.

(33) Meineke, P.; Rauen, U.; de Groot, H.; Korth, H. G.; Sustmann, R. *Biol. Chem.* **2000**, *381*, 575.

(34) Smith, R. C.; Tennyson, A. G.; Lim, M. H.; Lippard, S. J. *Org. Lett.* **2005**, *7*, 3573.

(35) Smith, R. C.; Tennyson, A. G.; Lippard, S. J. *Inorg. Chem.* **2006**, *45*, 6222.

(36) Lim, M. H.; Lippard, S. J. *J. Am. Chem. Soc.* **2005**, *127*, 12170.

(37) Lim, M. H.; Lippard, S. J. *Inorg. Chem.* **2006**, *45*, 8980.

(38) Lim, M. H.; Wong, B. A.; Pitcock, W. H.; Mokshagundam, D.; Baik, M. H.; Lippard, S. J. *J. Am. Chem. Soc.* **2006**, *128*, 14364.

(39) Lim, M. H.; Xu, D.; Lippard, S. J. *Nat. Chem. Biol.* **2006**, *2*, 375.

(40) Lim, M. H.; Lippard, S. J. *Acc. Chem. Res.* **2007**, *40*, 41.

(41) McQuade, L. E.; Pluth, M. D.; Lippard, S. J. *Inorg. Chem.* **2010**, *49*, 8025.

(42) McQuade, L. E.; Ma, J.; Lowe, G.; Ghatpande, A.; Gelperin, A.; Lippard, S. J. *Proc. Natl. Acad. Sci. U.S.A.* **2010**, *107*, 8525.

(43) McQuade, L. E.; Lippard, S. J. *Inorg. Chem.* **2010**, *49*, 7464.

(44) Pluth, M. D.; McQuade, L. E.; Lippard, S. J. *Org. Lett.* **2010**, *12*, 2318.

(45) Wang, S. H.; Han, M. Y.; Huang, D. J. *J. Am. Chem. Soc.* **2009**, *131*, 11692.

(46) Yan, X. Q.; Shang, Z. B.; Zhang, Z.; Wang, Y.; Jin, W. J. *Luminescence* **2009**, *24*, 255.

(47) Kim, J.-H.; Heller, D. A.; Jin, H.; Barone, P. W.; Song, C.; Zhang, J.; Trudel, L. J.; Wogan, G. N.; Tannenbaum, S. R.; Strano, M. S. *Nat. Chem.* **2009**, *1*, 473.

(48) Jin, H.; Heller, D. A.; Kim, J. H.; Strano, M. S. *Nano Lett.* **2008**, *8*, 4299.

(49) Jin, H.; Heller, D. A.; Kalbacova, M.; Kim, J.-H.; Zhang, J.; Boghossian, A. A.; Maheshri, N.; Strano, M. S. *Nat. Nano* **2010**, *5*, 302.

(50) Heller, D. A.; Baik, S.; Eurell, T. E.; Strano, M. S. *Adv. Mater.* **2005**, *17*, 2793.

(51) O'Connell, M. J.; Bachilo, S. M.; Huffman, C. B.; Moore, V. C.; Strano, M. S.; Haroz, E. H.; Rialon, K. L.; Boul, P. J.; Noon, W. H.; Kittrell, C.; Ma, J. P.; Hauge, R. H.; Weisman, R. B.; Smalley, R. E. *Science* **2002**, *297*, 593.

(52) Saito, R.; Dresselhaus, M. S.; Dresselhaus, G. *Physical Properties of Carbon Nanotubes*; Imperial College Press: London, 1998.

(53) Heller, D. A.; Jeng, E. S.; Yeung, T. K.; Martinez, B. M.; Moll, A. E.; Gastala, J. B.; Strano, M. S. *Science* **2006**, *311*, 508.

(54) Barone, P. W.; Parker, R. S.; Strano, M. S. *Anal. Chem.* **2005**, *77*, 7556.

(55) Barone, P. W.; Baik, S.; Heller, D. A.; Strano, M. S. *Nat. Mater.* **2005**, *4*, 86.

(56) Cognet, L.; Tsyboulski, D. A.; Rocha, J. D. R.; Doyle, C. D.; Tour, J. M.; Weisman, R. B. *Science* **2007**, *316*, 1465.

(57) Siitonen, A. J.; Tsyboulski, D. A.; Bachilo, S. M.; Weisman, R. B. *Nano Lett.* **2010**, *10*, 1595.

(58) Siitonen, A. J.; Tsyboulski, D. A.; Bachilo, S. M.; Weisman, R. B. *J. Phys. Chem. Lett.* **2010**, *1*, 2189.

(59) Heller, D. A.; Jin, H.; Martinez, B. M.; Patel, D.; Miller, B. M.; Yeung, T. K.; Jena, P. V.; Hobartner, C.; Ha, T.; Silverman, S. K.; Strano, M. S. *Nature Nanotechnol.* **2009**, *4*, 114.
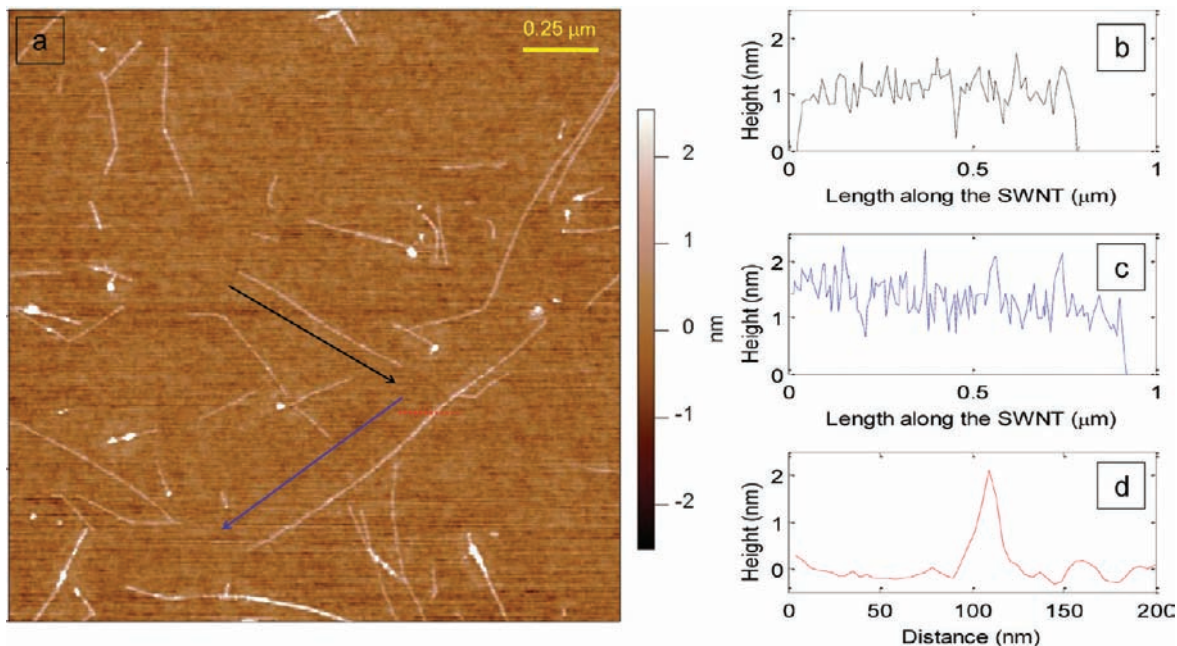
Figure 1. Atomic force microscopy (AFM) image of AT_{15}−SWNT, along with section and height analysis. (a) A typical AFM (tapping mode) image of AT_{15}−SWNT deposited on an oxygen plasma prewetted, silicon dioxide surface. (b, c) Height profile of the AT_{15}−SWNT along the length of the nanotube with arrows in the original AFM image (a) indicating the direction of the profiling (black arrow, b; blue arrow, c). The bands reach about 0.5−1 nm from the surface of the SWNT. (d) Height profile from left to right along the dotted red line in image a.

tion from each SWNT on the array. While we find the experimental ensemble detection limit for NO to be 300 nM for the entire array, the ability to detect NO generation locally with nanometer precision enables new enzymatic and cellular assays. This analysis is a significant improvement over approaches reported previously[48] in that information from a single fluorescence intensity trace (a single sensor) can inform the local concentration of the analyte.

2. Experimental Section

2.1. DNA Oligonucleotide/Polymer Nanotube Suspension. SWNTs were suspended with both $d(AT)_{15}$ and $d(GT)_{15}$ oligonucleotides using methods similar to the one published previously.[53] Briefly, HiPCO SWNTs purchased from Unidym were suspended with a 30-base (dAdT) or (dGdT) sequence of ssDNA (Integrated DNA Technologies) in a 2:1 DNA:SWNT mass ratio in 0.1 M NaCl in distilled water. Typical DNA concentration was 2 mg/mL. Samples were sonicated with a 3 mm probe tip (Cole-parmer) for 10 min at a power of 10 W, followed by benchtop centrifugation for 180 min (Eppendorf Centrifuge 5415D) at 16,100 RCF. Afterward, the supernatant was collected and the pellet discarded.

For suspension with other polymer materials, SWNTs were first suspended in a 2 wt % sodium cholate (SC) aqueous solution using previously published methods.[51,55] Briefly, 1 mg/mL Unidym SWNTs were added to 40 mL of 2 wt % SC in NanoPure H$_2$O and were sonicated with a 6 mm probe tip at 40% amplitude (∼12W) for 1 h in an ice bath. The resulting dark-black solution was ultracentrifuged in a SW32 Ti rotor (Beckman Coulter) at 153,700 RCF (max) for 4 h to remove unsuspended SWNT aggregates and catalyst particles. The desired polymer for SWNT suspension was then dissolved, at 1 wt %, in the SC−SWNT, and the mixture was placed in a 12−14 kD MWCO dialysis bag and dialyzed against 2 L of 1x Tris buffer (20 mM, pH 7.3) for 24 h to remove free SC and allow the polymer to self-assemble on the nanotube surface. The dialysis buffer was changed after 4 h to ensure SC removal.

The resulting suspensions were visually clear and were free of SWNT aggregates, indicating successful suspension.[60]

2.2. NO Solution. NO solution was obtained using a method similar to the one reported previously.[47] Briefly, 3 mL of phosphate buffer saline (PBS, 1x) was contained in a 5 mL round-bottom flask and sealed with a septum with two needles inserted providing an inlet and an outlet, respectively. After argon gas (Airgas) was purged for 2 h to remove dissolved oxygen in the buffer, nitric oxide gas (99.99%, Electronicfluorocarbons) was introduced for 20 min at an outlet pressure of 2 psi. The concentration of NO was measured using horseradish peroxidase assay.[28,61] Series dilution of NO solution was achieved by mixing concentrated NO solution with PBS buffer (argon prepurged for 2 h) in a pear-shaped flask (argon prepurged for 20 min). The syringe apparatus was purged with argon before usage.

2.3. Atomic Force Microscopy (AFM) Imaging. In this work, two different types of surfaces were used for AFM imaging for different purposes. In order to verify that the SWNT suspension yields individual SWNTs and to estimate the height of the wrapping on the SWNT surface, AT_{15}−SWNT was deposited on an oxygen plasma prewetted silicon dioxide surface. In this case, free DNA was removed from AT_{15}−SWNT suspension using spin column (MicrospinS-400HR columns, GE Healthcare), and the suspension was diluted to 7.5 mg/L concentration measured using UV−vis−NIR scanning spectrophotometer (UV-3101 PC Shimadzu). The concentration of SWNT was determined using absorbance at 632 nm with $\varepsilon = 0.036$ (mg/L)$^{-1}$ cm^{-1}. Oxygen plasma (Harrick Plasma) was applied to enhance the hydrophilicity of the silicon dioxide surface, assisting DNA−SWNT adsorption on the surface. The sample was then spin-coated to the silicon dioxide surface (LaureII Technology Corporation, model WS-650MZ-23NPP/LITE) for 1 min with ramp speed of 500 rpm and final speed of 2500 rpm. The resultant AFM images are shown in Figure 1 and Figure S1, Supporting Information.

(60) Barone, P. W.; Strano, M. S. *Angew. Chem.* **2006**, *118*, 8318.
(61) Kikuchi, K.; Nagano, T.; Hirobe, M. *Biol. Pharmacol. Bull.* **1996**, *19*, 649.

In order to verify that SWNT is individually deposited on a solid substrate, AFM images (Figure S2, Supporting Information) were taken with SWNT samples that were deposited on silicon dioxide surface pretreated with (3-aminopropyl)triethoxysilane (APTES). For sample preparation, the same procedure (See Section 2.6) was used as in the sample required for fluorescence detection, except that the silicon dioxide surface was used for depositing instead of the glass slide, in order to obtain a smoother surface for AFM imaging. All the AFM images were taken using Asylum Tapping/ AC mode soft tips (AC240TS).

2.4. Measurement of SWNT Photoluminescence (PL). Setup for High Throughput Screening Assay. All polymer-wrapped SWNT solutions were diluted using buffer to a final SWNT concentration of 2 mg/L. The following analytes were initially dissolved in DMSO, including ATP, cAMP, creatinine, D-aspartic acid, glycine, L-citrulline, L-histidine, quinine, and sodium pyruvate; all other analytes were dissolved in water. Analyte solutions were added to the SWNT, such that the final DMSO concentration was 1 vol %, the mixture was incubated for 1 h and the resulting SWNT PL was measured with a home-built near-infrared (nIR) fluorescence microscope. Fluorescence measurement upon exposure NO was measured using previously published methods.[47] The high-throughput screening setup is shown in Figure S3, Supporting Information. Briefly, a Zeiss AxioVision inverted microscope was coupled to a Princeton Instruments InGaAs OMA V array detector through a PI Acton SP2500 spectrometer. Sample excitation was from a 785 nm photodiode laser, 450 mW at the source, and 150 mW at the sample.

2.5. Screening of AT_{15}−SWNT against Other Nine Reactive Oxygen and Nitrogen Species. Sodium peroxynitrite and Angeli's salt were purchased from Cayman Chemical, and other chemicals in this experiment was purchased from Sigma. Stock solution of NO_2^-, NO_3^-, H_2O_2, and ClO^- were prepared by dissolving them in water at 6 mM; $ONOO^-$ and Angeli's salt were first dissolved at 6 mM in solutions of 0.3 M of NaOH and 0.01 M NaOH, respectively. O_2^- was prepared following a procedure in the literature.[62] Briefly, an excess amount of KO_2 was added to DMSO, and the mixture was vortexed followed by centrifugation to remove the pellet. The resultant supernatant yields a stock solution of 3.6 mM O_2^-. Analyte solutions were added to the SWNT (2 mg/L in 50 mM PBS, pH = 7.4), such that the final concentration was 60 μM. The response was monitored for 10 min after addition. Hydroxyl radicals were generated using Fenton's reaction, where H_2O_2 and $FeSO_4$ (60/0.6, 300/3, and 1000/10 μM as final concentration) were added into the SWNT solution, and the reaction was monitored for the first 10 minutes, and again 12 hours after reagent addition. Rose bengal was used to generate singlet oxygen using a similar procedure as described previously.[49,63] Briefly, the solution of AT_{15}−SWNT (2 mg/L) was exposed to 60 μM of rose bengal and excited at 560 nm to generate singlet oxygen. The SWNT fluorescence response was recorded by quickly switching the excitation source at the end of every minute to a 785 nm laser (same as described in section 2.4) for 3 s. Repeating this cycle, the response was monitored for 10 min, at the end of which, the 560 nm-excitation source was turned off, and three additional spectra excited using 785 nm were taken every minute.

2.6. Microscopy and Data Collection for Single Molecule NO Detection. AT_{15}−SWNTs were deposited onto a Petri dish pretreated with APTES (Figure 6a,b) substrate and washed three times to remove suspended SWNT as well as free DNA in the sample. The electrostatic interaction between AT_{15}−SWNT and APTES is enough to keep the construct stable at physiological pH. The microscopy technique is similar to that reported in the literature[48] (Figure 6a). Briefly, samples were excited by a 658 nm laser (LDM-OPT-A6−13, Newport Corp) at 33.8 mW. The

fluorescence of AT_{15}−SWNT was imaged and monitored in real time through a 100× TIRF objective for hours using an inverted microscope (Carl Zeiss, Axiovert 200), with a 2D InGaAs array (Princeton Instruments OMA 2D) attached. Movies were acquired at 0.2 s/frame using the WinSpec data acquisition program (Princeton Instruments). Before the actual experiment, a control movie (same movie length as the experiment movie) was taken to ensure a stable baseline. In the experiment, NO in PBS (1x, pH 7.4) buffer was injected through a fine hole, allowing minimal exposure to air.

3. Results and Discussion

3.1. NO Selective PL Quenching of $d(AT)_{15}$ DNA-Wrapped SWNT. Individual suspension of SWNT encapsulated in $d(AT)_{15}$ DNA (AT_{15}−SWNT) is confirmed by AFM (Figures 1 and S1). As depicted in the molecular model of Figure 2a and Figure 2b, it is generally accepted that the nucleobases of the DNA stack on the sidewall of the SWNT, while the sugar−phosphate backbone extends away from the surface. This is consistent with both experimental evidence, including AFM[64,65] and optical absorption data,[66] as well as molecular dynamics simulations[67−71] reported to date. Through $\pi-\pi$ stacking of the bases on the sidewall of the SWNT, the phosphate backbone of the DNA is exposed to water, allowing SWNT to remain colloidally stable.

We utilized a custom-designed near-infrared SWNT fluorescence imaging microscope and spectrometer to characterize emission (Figure S3). Upon 785 nm laser excitation, near-infrared (nIR) emission of AT_{15}−SWNT can be captured by a 1D InGaAs spectrometer (Figure 2c,d). In order to determine the SWNT species present in the SWNT suspension, a 2D excitation−emission profile was taken as described previously[72] (Figure S4, Supporting Information). By using this plot to identify the emission peak center of each SWNT species, the corresponding 1D fluorescence spectrum can be deconvoluted into individual species contributions (Figure 2c). Detailed discussion of the spectral deconvolution can be found in the Supporting Information.

We find that the DNA sequence in AT_{15}−SWNT is unique in its ability to detect selective quenching from primarily NO when compared with a large panel of potentially interfering species. Upon exposure to NO (60 μM, in 1x PBS), the fluorescence of all observed SWNT species is completely quenched (Figure 2d). We designed an automated, high-throughput screening assay whereby fluorescence modulation of DNA oligonucleotides, peptides, and other synthesized polymer-encapsulated SWNTs is monitored upon exposure to 36 biological molecules (Table S1). These molecules serve to

(62) Reiter, C. D.; Teng, R.-J.; Beckman, J. S. *J. Biol. Chem.* **2000**, *275*, 32460.

(63) Mizukawa, H.; Okabe, E. *Br. J. Pharmacol.* **1997**, *121*, 63.

(64) Zheng, M.; Jagota, A.; Strano, M. S.; Santos, A. P.; Barone, P.; Chou, S. G.; Diner, B. A.; Dresselhaus, M. S.; McLean, R. S.; Onoa, G. B.; Samsonidze, G. G.; Semke, E. D.; Usrey, M.; Walls, D. J. *Science* **2003**, *302*, 1545.

(65) Jin, H.; Jeng, E. S.; Heller, D. A.; Jena, P. V.; Kirmse, R.; Langowski, J.; Strano, M. S. *Macromolecules* **2007**, *40*, 6731.

(66) Hughes, M. E.; Brandin, E.; Golovchenko, J. A. *Nano Lett.* **2007**, *7*, 1191.

(67) Zheng, M.; Jagota, A.; Semke, E.; Diner, B.; McLean, R.; Lustig, S.; Richardson, R.; Tassi, N. *Nat. Mater.* **2003**, *2*, 338.

(68) Meng, S.; Maragakis, P.; Papaloukas, C.; Kaxiras, E. *Nano Lett.* **2006**, *7*, 45.

(69) Manohar, S.; Tang, T.; Jagota, A. *J. Phys. Chem. C* **2007**, *111*, 17835.

(70) Johnson, R. R.; Johnson, A. T. C.; Klein, M. L. *Nano Lett.* **2008**, *8*, 69.

(71) Johnson, R. R.; Kohlmeyer, A.; Johnson, A. T. C.; Klein, M. L. *Nano Lett.* **2009**, *9*, 537.

(72) Bachilo, S. M.; Strano, M. S.; Kittrell, C.; Hauge, R. H.; Smalley, R. E.; Weisman, R. B. *Science* **2002**, *298*, 2361.
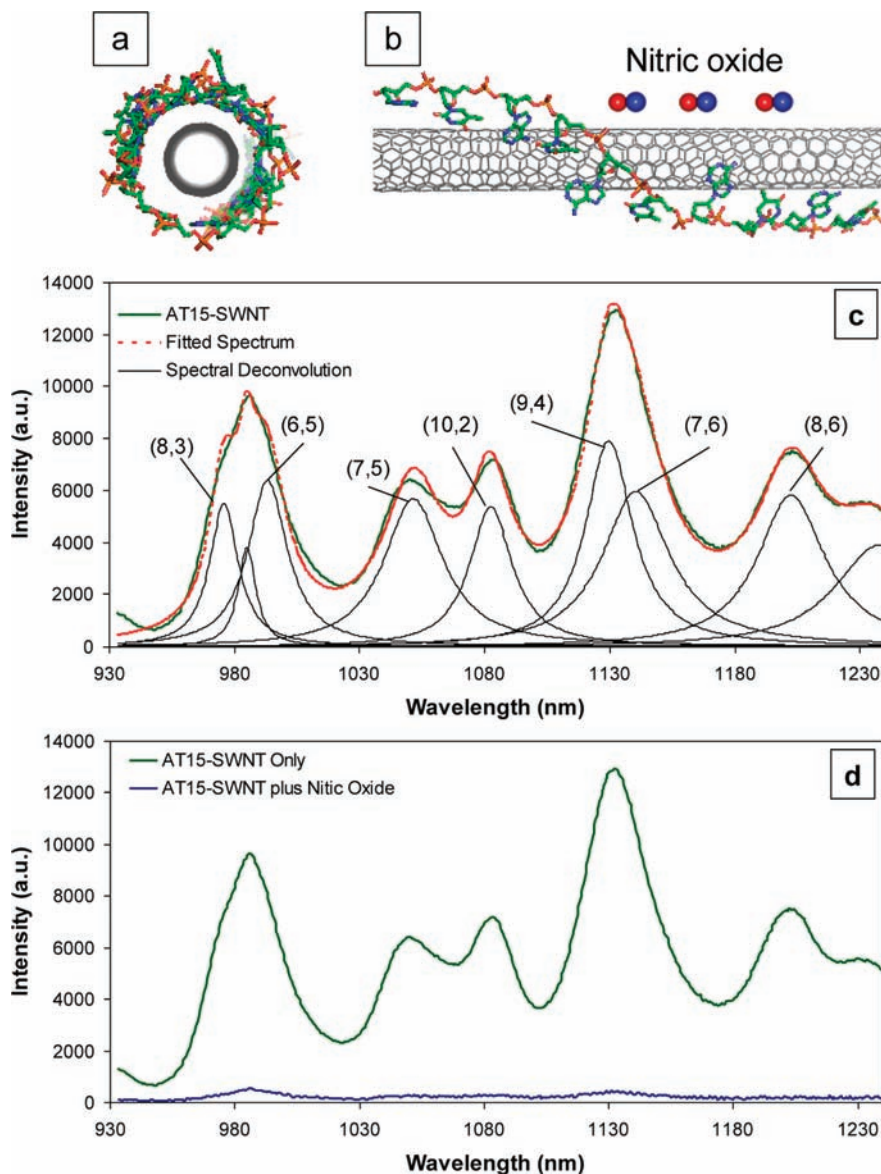
Figure 2. The optical response of $d(AT)_{15}$ DNA oligonucleotide wrapped SWNT (AT_{15}–SWNT) upon exposure to NO. (a and b) Front and side schematic views of one of the several binding structures of AT_{15}–SWNT simulated from a HyperChem simulation package. Bases of the DNA stack on the sidewall of the SWNT, and the sugar–phosphate backbone extends away from the surface. (c) The nIR fluorescence spectrum (solid green) of AT_{15}–SWNT recorded with a $50\times$ objective upon 785 nm laser excitation (150 mW at the sample). The spectral deconvolution reveals seven nanotube species and a Raman peak (solid black), with the sum of these contributions (dotted red) matching the profile of the actual data. (d) Complete quenching (solid blue) of AT_{15}–SWNT fluorescence is observed when the SWNT sample is exposed to NO (60 μM, in 1x PBS).

fingerprint and probe differences in response to distinct polymer–SWNT complexes. We conclude from this screening that NO exclusively quenches this complex, with essentially no response from other analyte species in the library (Figure 3). This is in marked contrast to what is seen for an electrostatically neutral polymer, polyvinyl alcohol (PVA–SWNT), whose fluorescence is not affected by NO (Figure 3d). Note that this is despite the fact that concentrations of the majority of library species ($\sim$500 μM) are higher than that of NO (60 μM) in the screening, while others are constrained by their solubility. Removing free DNA from the SWNT suspension has little effect on the selectivity (Figure S5, Supporting Information). We conclude that the wrapping polymer is responsible for the observed selectivity. For instance, $d(GT)_{15}$ differs from $d(AT)_{15}$ by a replacement of one base type, but its response is very different, with quenching from dopamine, histamine, L-ascorbic acid, melatonin, NADH, and riboflavin (Figure 3b). Other

$d(AT)_{15}$ variants including $d(AAAAT)_6$, $d(AAATT)_6$, $d(AAT)_{10}$, $d(ATT)_{10}$, $d(AAAT)_7$, $d(AATTT)_6$, and $d(AATT)_7$ show response profiles similar to $d(AAT)_{10}$ (Figure 3c), where additional molecules besides NO also greatly modulate SWNT fluorescence. Of all AT variants studied, AT_{15}–SWNT appears to be the only DNA–SWNT complex that shows a selective response toward NO over riboflavin (Figure 3e). Such a selective response of SWNT imparted by an adsorbed DNA molecule has been reported previously. For instance, it has been shown that certain DNA sequences attached to SWNT can recognize specific odor molecules through a change in electronic resistance.[73-75] Moreover, while PVA–SWNT shows a quenching response to dopamine, similar to a typical

(73) Khamis, S. M.; Johnson, R. R.; Luo, Z. T.; Johnson, A. T. C. *J. Phys. Chem. Solids* **2010**, *71*, 476.
(74) Johnson, A. T. C.; Khamis, S. M.; Preti, G.; Kwak, J.; Gelperin, A. *IEEE Sens. J.* **2010**, *10*, 159.
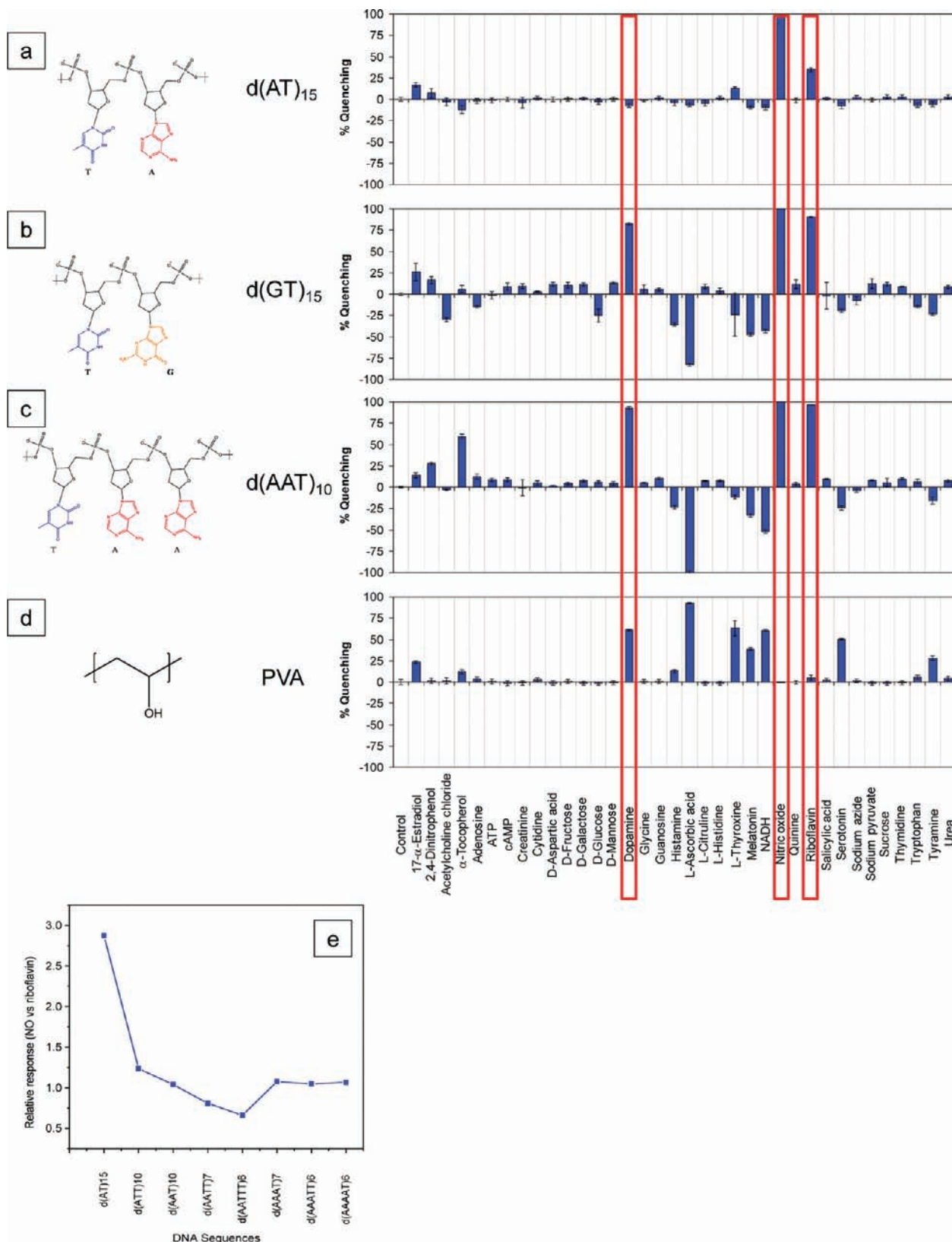
Figure 3. Selective NO response of AT_{15}–SWNT and high throughput screening of polymer–SWNT complexes. Bar charts represent the percentage of quenching $(1 - I/I_0)$ of the (7,5) nanotube species when wrapped in four different polymers: $d(AT)_{15}$ DNA (a), $d(GT)_{15}$ DNA (b), $d(AAT)_{10}$ DNA (c), and polyvinyl alcohol (PVA, d) upon exposure to the 36 analytes. Red boxes highlight the responses of the four types of polymer–SWNT complexes to dopamine, riboflavin, and NO. (e) Relative quenching response of DNA encapsulated (7,5) SWNT upon exposure to 60 μM NO vs 100 μM riboflavin, or $(1 - I/I_0)_{NO}/(1 - I/I_0)_{riboflavin}$.

DNA response profile, its fluorescence is enhanced when exposed to reducing agents including NADH, L-ascorbic acid, and melatonin, which is in contrast to the DNA–SWNT response profile.

We attribute the selectivity of d(AT)$_{15}$−SWNT to potentially three distinct components: redox selectivity, nonradiative energy loss, and steric hindrance. Addressing the first, we note that most of the responses shown in Figure 3 are the result of interaction between redox-active molecules and polymer−SWNT complexes. For instance, the LUMO levels of NO (−0.5 V)[76] and riboflavin (−0.318 V)[77] are close to the conduction bands of the SWNT species utilized in this work.[78] Therefore, it is plausible that they cause a fluorescence decrease through excited-state electron quenching.[79] Moreover, the fluorescence enhancements caused by reducing agents including NADH, L-ascorbic acid, and melatonin on DNA−SWNT are likely because NADH reduces the DNA wrapping whose LUMO band is below the Fermi level of semiconducting SWNTs,[80] resulting in a recovery of photoluminescence that is prequenched by DNA.[79] More specifically, HOMO electrons of NADH can compete with SWNT excited state electrons for the vacancies at the LUMO level of DNA, inhibiting SWNT excitons from quenching (Figure 4a). We also noticed that DNA−SWNT fluorescence enhancement after NADH addition is weakened as the energy gap between the conduction band of SWNT and the LUMO of DNA molecule decreases, or generally as the diameter of the SWNT increases (Figure 4e), supporting the fluorescence enhancing mechanism we proposed. In contrast, the mechanism of PVA−SWNT fluorescence quenching caused by reducing agents has not been extensively studied, although others have reported similar observations.[81] We hypothesize that NADH and other reducing agents donate electrons directly to the conduction bands of PVA−SWNT, and extra electrons in the conduction bands can then quench excitons through a nonradiative Auger recombination[82,83] (Figure 4b). An attempt to assign the absolute values of oxidation potential measured of NADH (0.282 V),[84] melatonin (0.95 V),[85] and L-ascorbic acid (0.74 V)[86] in the SWNT potential scale[81,87−89] results in the potential levels of those molecules lying below the conduction bands and above the valence bands of SWNT, and we therefore expect to see an increase in electron density in the SWNT valence bands upon addition of those analytes. However, upon exposure to the analytes, experimentally measured absorption spectra of both PVA−SWNT and DNA−SWNT remain invariant (Figure S6, Supporting Information). This inconsis-tency may reflect the fact that reported oxidation potentials are measured through voltammetry where complete electron transfer and the formation of new adducts are involved, whereas electron transfer between SWNT and the cited molecules appears reversible, suggesting a weaker, electron-sharing mechanism between the SWNT surface and the adsorbates. Hence, we only considered the relative oxidation potentials of those molecules, and constructed a potential plot that summarizes redox level of the SWNT, encapsulating polymer, and the interfering molecules (Figure 4c).

Redox potentials cannot alone account for selectivity, however. Counterintuitively, dopamine appears to quench all polymer−SWNT complexes except AT$_{15}$−SWNT, although its HOMO level is between NADH and L-ascorbic acid. We consider that dopamine may behave as a defect site on the SWNTs, which forms a nonradiative energy 'sink' of excitons, causing fluorescence quenching.[90] Because the size of dopamine (Figure 4d) is small compared to the anticipated gaps in the DNA adsorbed phase, and the aromatic ring structure can π−π stack on the SWNT surface, this hypothesis is plausible. A polymer that prohibits direct adsorption of dopamine to the SWNT surface, for example, can eliminate this response.

All redox related responses discussed above appear to be attenuated in the case of AT$_{15}$−SWNT. We suspect that the sequence adopts a conformation on the nanotube surface that results in steric exclusion of most analytes except NO. This can be the case if d(AT)$_{15}$ forms closely spaced bands along the circumference of the tube, thereby blocking the adsorption of molecules greater in size than NO. Sequence-dependent variability in DNA adsorption configuration is not unusual and is likely to be one of the factors involved in utilizing DNA sequences to separate carbon nanotube by chirality.[64,91] In our work, AFM micrographs of AT$_{15}$−SWNT (Figure 1) suggest AT$_{15}$ wraps SWNT uniformly with heights between 0.5−1 nm above the surface of SWNT, although we were unable to resolve regular helical patterns that have been observed previously for other sequences.[64,65] Currently, we are not able to prove directly that d(AT)$_{15}$ forms more closely spaced bands on SWNT compared to other AT variants or DNA sequences. However, the concept of a sequence or structure induced steric selectivity is also indirectly supported by the fact that AT$_{15}$−SWNT and PVA−SWNT show deviations from the typical quenching pattern observed with other sequences. In particular, dopamine and riboflavin fail to cause quenching in the cases of AT$_{15}$−SWNT and PVA−SWNT, respectively. The relative sizes of these molecules (approximately 9 × 9 × 3 Å for dopamine and 10 × 12 × 4 Å for riboflavin, Figure 4d) mean that a void in the adsorbed phase of at least 1 nm needs to form in order to have direct energy transfer from the SWNT to the molecule. The unadsorbed portion of the wrapping molecule then interacts with the adsorbed phase creating the binding site, and both of these factors can allow for steric selectivity.

The case of NO adsorption on PVA−SWNT is unusual. Because of its small size, NO tends to quench nearly every complex we have tested to date. However, for PVA−SWNT, there is no response. It is possible that NO reacts directly with the PVA itself, via exposed hydroxyl groups, for example. However, this would not itself explain the lack of response, since quenching would be apparent as soon as these sites were

(75) Johnson, A. T. C.; Staii, C.; Chen, M.; Khamis, S.; Johnson, R.; Klein, M. L.; Gelperin, A. *Semicond. Sci. Technol.* **2006**, *21*, S17.

(76) Bartberger, M. D.; Liu, W.; Ford, E.; Miranda, K. M.; Switzer, C.; Fukuto, J. M.; Farmer, P. J.; Wink, D. A.; Houk, K. N. *Proc. Natl. Acad. Sci. U.S.A.* **2002**, *99*, 10958.

(77) Anderson, R. F. *Biochim. Biophys. Acta* **1983**, *722*, 158.

(78) References for potential levels in this work are with respect to normal hydrogen electrode (NHE).

(79) Satishkumar, B. C.; Brown, L. O.; Gao, Y.; Wang, C.-C.; Wang, H.-L.; Doorn, S. K. *Nat. Nano* **2007**, *2*, 560.

(80) Shoda, M.; Bandow, S.; Maruyama, Y.; Iijima, S. *J. Phys. Chem. C* **2009**, *113*, 6033.

(81) Tanaka, Y.; Hirayama, K.; Niidome, Y.; Nakashima, N. *Chem. Phys. Lett.* **2009**, *482*, 114.

(82) Wang, F.; Dukovic, G.; Knoesel, E.; Brus, L. E.; Heinz, T. F. *Phys. Rev. B* **2004**, *70*, 241403.

(83) Dukovic, G.; White, B. E.; Zhou, Z.; Wang, F.; Jockusch, S.; Steigerwald, M. L.; Heinz, T. F.; Friesner, R. A.; Turro, N. J.; Brus, L. E. *J. Am. Chem. Soc.* **2004**, *126*, 15269.

(84) Anderson, R. F. *Biochim. Biophys. Acta* **1980**, *590*, 277.

(85) Mahal, H. S.; Sharma, H. S.; Mukherjee, T. *Free Radic. Biol. Med.* **1999**, *26*, 557.

(86) Turyan, Y. I.; Kohen, R. *J. Electroanal. Chem.* **1995**, *380*, 273.

(87) Tanaka, Y.; Hirana, Y.; Niidome, Y.; Kato, K.; Saito, S.; Nakashima, N. *Angew. Chem., Int. Ed.* **2009**, *48*, 7655.

(88) O'Connell, M.; Eibergen, E.; Doorn, S. *Nat. Mater.* **2005**, *4*, 412.

(89) Zheng, M.; Diner, B. A. *J. Am. Chem. Soc.* **2004**, *126*, 15490.

(90) Wang, F.; Dukovic, G.; Brus, L. E.; Heinz, T. F. *Phys. Rev. Lett.* **2004**, *92*, 177401.

(91) Tu, X.; Manohar, S.; Jagota, A.; Zheng, M. *Nature* **2009**, *460*, 250.
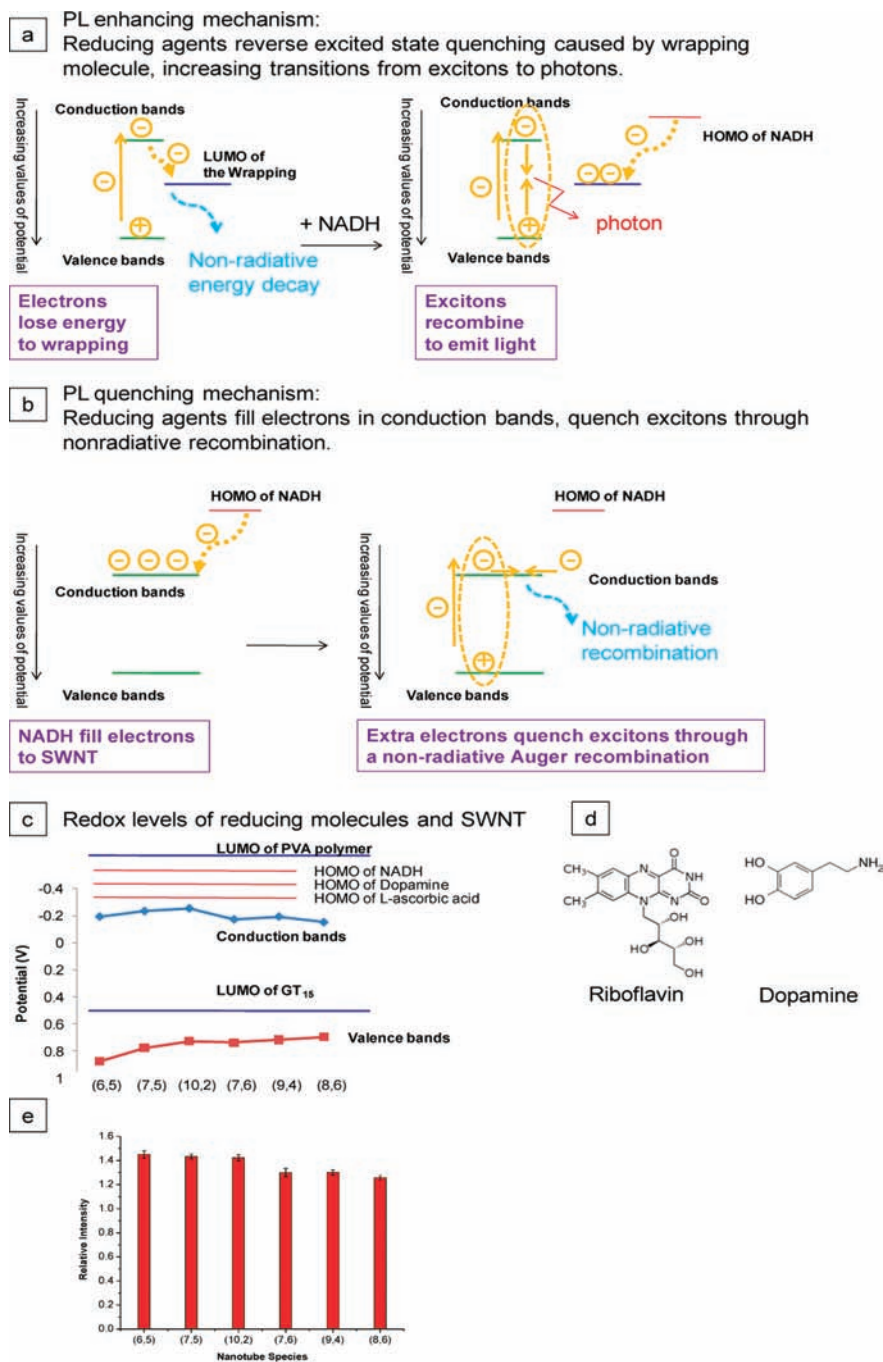
a PL enhancing mechanism:
Reducing agents reverse excited state quenching caused by wrapping molecule, increasing transitions from excitons to photons.

b PL quenching mechanism:
Reducing agents fill electrons in conduction bands, quench excitons through nonradiative recombination.

c Redox levels of reducing molecules and SWNT

d Riboflavin   Dopamine

e

Figure 4. Illustration of the contribution of redox interactions to the selectivity of the polymer- SWNT complexes. (a) A plausible mechanism for SWNT fluorescence enhancement. In this process, polymers adsorbed on the SWNT surface initially act as exciton quenchers, since excited electrons decay to the LUMO level of the polymer wrapping. When NADH is added to the solution, it donates electrons to the polymer LUMO level, thereby preventing exciton decay. This results in a subsequent enhancement of the SWNT photoluminescence. (b) A plausible quenching mechanism. NADH and other reducing agents donate electrons directly to the conduction bands of polymer−SWNT, and extra electrons in the conduction bands quench excitons through a nonradiative Auger recombination. (c) Potential levels of SWNT, wrapping polymers, and redox-active molecules. Potentials of SWNT conduction and valence bands are obtained from the several literature sources,[81,87−89] and DNA doping levels are estimated from ref 80. The HOMO levels of NADH, dopamine, and L-ascorbic acid are plotted relative to the potential of the SWNT. (d) Molecular structure of riboflavin and dopamine. (e) Relative intensity (I/I_0) of GT_{15}−SWNT exposed to NADH compared to the control where no analytes were added, as a function of SWNT species.

saturated. Another possibility may involve a subsequent pore blocking due to the formation of organo-nitrite after reaction with NO.[92] This potential mechanism is a topic for future work. Regardless of mechanism, the obvious selectivity demonstrated in this case, and the above examples, clearly indicates that the polymer adsorbed phase on SWNT strongly influences the

apparent selectivity of the complex, and this has significant implications for all sensor applications of carbon nanotubes.

3.2. Selectivity of AT_{15}−SWNT against Other Reactive Oxygen and Nitrogen Species. To examine the biological relevance of this platform, the responses of AT_{15}−SWNT were screened against nine reactive oxygen (ROS) and nitrogen species (RNS). Once exposed to 60 μM of each analyte, the SWNTs show little or no response to NO_2^-, NO_3^-, HNO, H_2O_2, OH·(hydroxyl
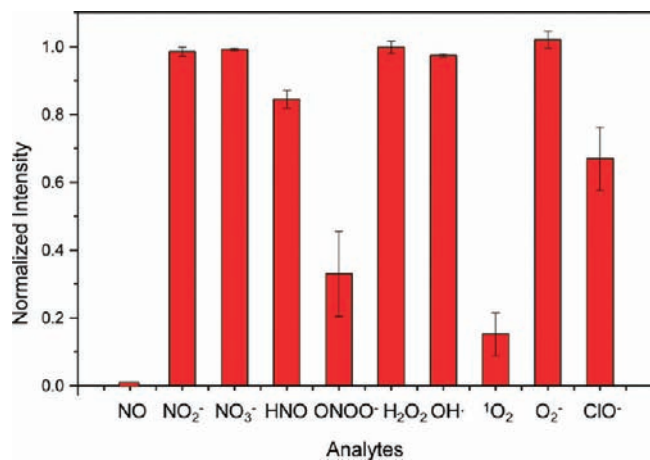
(92) Tarte, P. *J. Chem. Phys.* **1952**, *20*, 1570.

Figure 5. Fluorescence intensity (I/I_0, intensity/initial intensity) of (7,5) species of $AT_{15}-SWNT$ measured 10 min after addition of 60 μM of each analyte. SWNT is at 2 mg/L in PBS (pH = 7.4, 50 mM).

radical), O_2^-(superoxide), and ClO^-, but quench in response to peroxynitrite ($ONOO^-$) and singlet oxygen ($^1O_2$) (Figure 5 and Figure S7, Supporting Information). However, interference from peroxynitrite and singlet oxygen with the sensor is expected to be minimal, if any, for the applications that we wish to pursue. The reported half-life of NO in a biological system is on the order of seconds,[93,94] and the main contribution of its short-lived lifetime is its reactivity with hemoglobin. While 0.5 μM NO in aqueous solution has a half-life of $10-15$ s when equilibrated with room air,[95] at a much lower concentration (0.01–1 μ M, biologically relevant concentration), its half-life is much longer (500 s).[96] In contrast, the lifetime of singlet oxygen in water without any interference is only 4 μs,[97–99] which is over 1000 times shorter-lived than NO. In our single-molecule detection scheme, the transitions are recorded at 0.2 s/frame. Adsorbed singlet oxygens, if any, are more likely to be decomposed before the quenching transition is recorded.

Peroxynitrite self-decomposes at physiological pH, with a half-life of 2 s.[100] In the presence of dissolved CO_2, the half-life is significantly decreased.[101,102] In addition to the shorter lifetime of peroxynitrite compared to NO, our sensor exhibits a much more sensitive response to NO than to peroxynitrite. The response time for NO is $t_{1/2} = 1.1$ s, but 28 s to peroxynitrite (Figure S8, Supporting Information), which is also much longer than the half-life of peroxynitrite. Therefore, it is highly unlikely that a trace amount of peroxynitrite in a biological system would interfere with NO detection.

3.3. Arrays of SWNT Reporting Single Molecule Adsorption of NO. A NO sensing SWNT array was realized by depositing individual $AT_{15}-SWNT$ on an APTES-treated, glass-bottomed

Petri dish through electrostatic interactions (Figure 6a,b). This tethering appears to enhance the efficiency of SWNT deposition and also keeps the complex immobilized on the glass slide during multiple rinsing steps. Upon 658 nm laser excitation, the SWNTs on the array emit stable near-infrared light, which is collected in real-time by a near-infrared two-dimensional array detector at a frame rate of 0.2 s/frame. In the fluorescence image (Figure 6c), each individual $AT_{15}-SWNT$ is shown as a diffraction-limited fluorescent spot of approximately 2×2 pixel size, with each pixel representing an area of 290×290 nm^2. The AFM micrographs (Figure S2, Supporting Information) confirm that $AT_{15}-SWNT$ is individually deposited on the substrate. Once the array is exposed to NO, stepwise photoluminescence quenching of each SWNT in the array is observed over time (Figure 6d, red). In order to obtain meaningful results, the dark current is first obtained by averaging the camera signal over a 20×20 pixel area that does not contain SWNT and then subtracting it from each trace. Mechanistically, as the NO adsorbs on the accessible area of the SWNT, excitons that form within the exciton excursion radius of the NO adsorption site (one exciton diffusion length) are quenched. Therefore, even sparse adsorption of NO on the SWNT causes a stepwise decrease in the SWNT fluorescence. We have reported similar observations for H_2O_2[48,49] and $Fe(CN)_6,^{3-}$[48] while others have investigated H^+ [56] and diazonium salts.[56–58] Each observed quenching step reports a single molecule NO adsorption event, and each fluorescence enhancing step reflects a single desorption event. Consider a single SWNT being divided into N segments, each of which is approximately the size of the exciton-diffusion length.[56–58] At any instant, we have the reaction,

$$NO + \theta \underset{k_d}{\overset{k_a}{\rightleftharpoons}} \theta* \qquad (1)$$

where k_a and k_d are defined as the single-site adsorption and desorption rates of NO on SWNT, respectively. θ and $\theta*$ refer to empty and NO-occupied sites, respectively. Mass action of reaction 1 reveals:

$$\frac{d\theta}{dt} = -(k_a[NO])\theta + k_d(\theta*)$$
$$\theta + \theta* = N \qquad (2)$$

where N is the total number of sites on the SWNT. At the NO concentration range we are testing, it is valid to assume that NO adsorption on the SWNT does not change its bulk concentration; therefore, k_a and [NO] can be grouped into one variable, k_a', and it satisfies,

$$k_a' = k_a[NO] \qquad (3)$$

Although both k_a' and k_d will affect the fluorescence response, we are more interested in k_a' because it provides a direct measure of NO concentration. The concentration of NO determines both the degree of quenching of the fluorescence over the observation time as well as the rate. The representative traces in Figure 6d indicate that within 600 s, around 40%, 60%, 100%, and 100% of quenching were observed at steady state when the sensor was exposed to 0.16 μM, 0.78 μM, 3.9 μM, and 19.4 μM of NO, respectively. In addition, 100% quenching of the SWNT occurs much faster in the case of 25 μM exposure than that of the 5 μM exposure, as expected. Moreover, only at low concentration were desorption steps even observed which indicates that k_a' becomes diminished as concentration of NO decreases, as expected

(93) Bates, J. N. *Neuroprotocols* **1992**, *1*, 99.
(94) Kelm, M. *Biochim. Biophys. Acta* **1999**, *1411*, 273.
(95) Clancy, R. M.; Miyazaki, Y.; Cannon, P. J. *Anal. Biochem.* **1990**, *191*, 138.
(96) Wink, D. A.; Darbyshire, J. F.; Nims, R. W.; Saavedra, J. E.; Ford, P. C. *Chem. Res. Toxicol.* **1993**, *6*, 23.
(97) Lindig, B. A.; Rodgers, M. A. J.; Schaap, A. P. *J. Am. Chem. Soc.* **1980**, *102*, 5590.
(98) Egorov, S. Y.; Kamalov, V. F.; Koroteev, N. I.; Krasnovsky, A. A.; Toleutaev, B. N.; Zinukov, S. V. *Chem. Phys. Lett.* **1989**, *163*, 421.
(99) Rodgers, M. A. J.; Snowden, P. T. *J. Am. Chem. Soc.* **1982**, *104*, 5541.
(100) Beckman, J. S.; Beckman, T. W.; Chen, J.; Marshall, P. A.; Freeman, B. A. *Proc. Natl. Acad. Sci. U.S.A.* **1990**, *87*, 1620.
(101) Radi, R. *Chem. Res. Toxicol.* **1998**, *11*, 720.
(102) Romero, N.; Denicola, A.; Souza, J. M.; Radi, R. *Arch. Biochem. Biophys.* **1999**, *368*, 23.
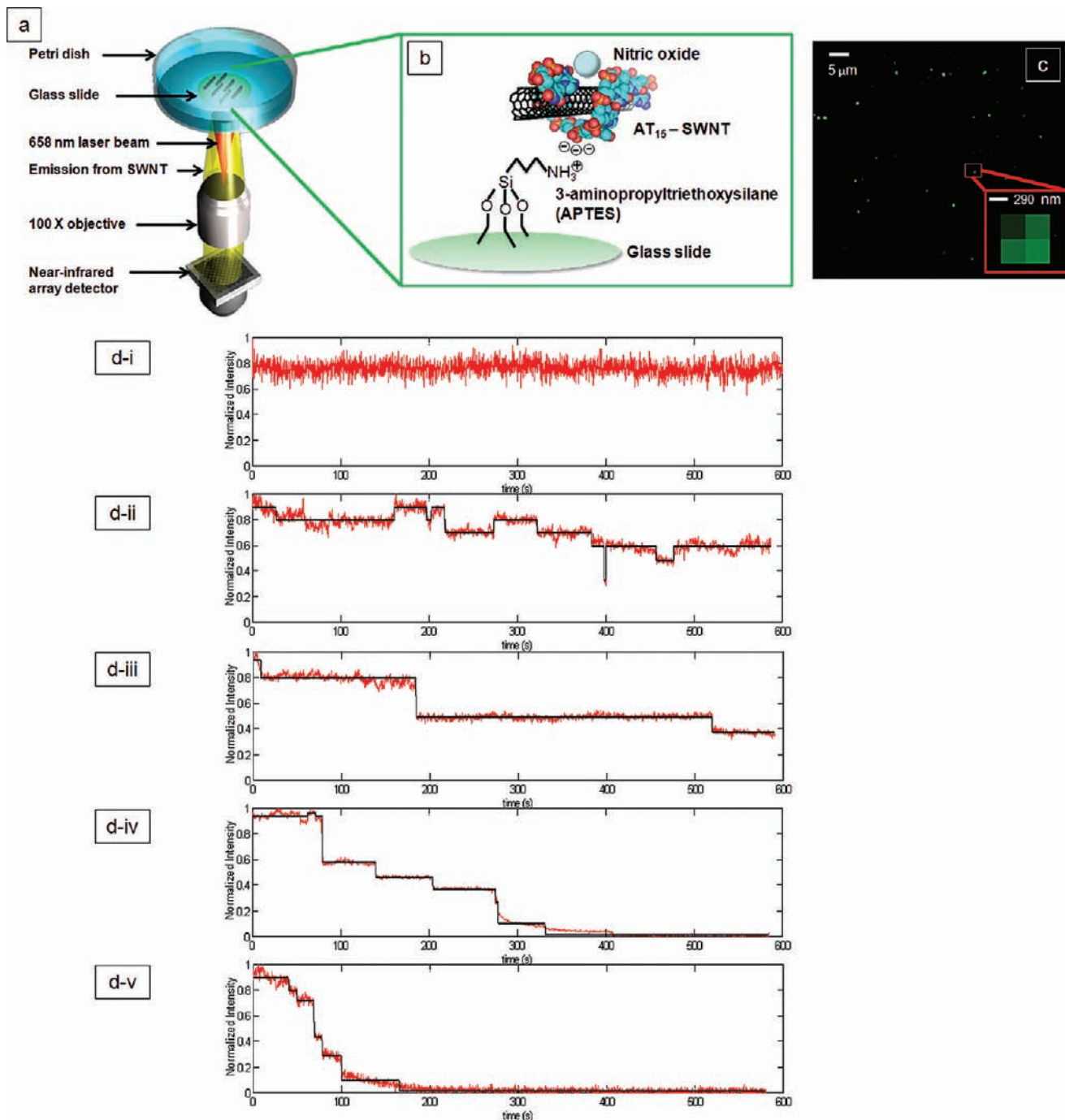
Figure 6. Fluorescence-based SWNT array capable of detecting NO. (a) Schematic of the microscope setup. A 658 nm laser beam (red) excites at the SWNT array deposited on the glass-bottomed Petri dish. The emission light (yellow) is collected by a near-infrared array detector through a $100\times$ TIRF objective mounted on an inverted microscope. (b) Schematic of the SWNT array: individual AT_{15}−SWNT complexes are deposited on the Petri dish, which is pretreated by (3-aminopropyl)triethoxysilane (APTES), through electrostatic interaction. (c) A representative near-infrared fluorescence image of the individual AT_{15}−SWNT deposited on the glass-bottomed Petri dish. The inset shows a near-infrared fluorescence image of a 2×2 pixel, diffraction-limited spot representing the fluorescence of an individual SWNT on the glass slide. The laser power at the sample is 33.8 mW. (d) Representative fluorescence time-trace (red) of a diffraction-limited spot (2×2 pixels) after being exposed to NO ($t = 0$ s) at five different concentrations (d-i, 0 μM, d-ii, 0.16 μM, d-iii, 0.78 μM, d-iv, 3.9 μM, d-v, 19.4 μM) and fitted traces (chi-squared error-minimizing step-finding algorithm, black). Each trace is normalized by the difference between the starting intensity and the dark-current intensity, and the latter is obtained through averaging intensity over a 20×20 pixel spot that does not contain any SWNT.

from eqs 2 and 3. These observations motivate the adoption of a generic analysis capable of extracting the local NO concentration directly from the transient quenching response.

3.4. Stochastic Analysis Using the Maximum Likelihood Estimation (MLE) for a Birth-and-Death Process. Previously, we investigated H_2O_2 as a quenching molecule over a film of collagen-wrapped SWNT with an observation time of 3000 s.[48]

Briefly, we first used *Hidden Markov Modeling* (HMM)[48,103] to distinguish actual stepwise transitions from noise in the fluorescence time-traces. Then, we converted transitions from all the traces (usually 100 traces) into an average transition probability matrix which can be used to estimate k'_a and k_d. One

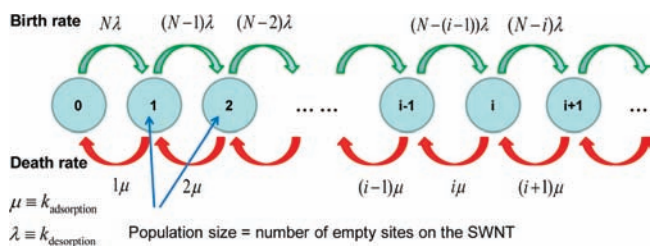(103) McKinney, S. A.; Joo, C.; Ha, T. *Biophys. J.* **2006**, *91*, 1941.

Figure 7. State transition-rate diagram of the birth-and-death process. The numbers in the circle indicate the states, or the population sizes of the birth-and-death process at any instant, t, and in the case of single-molecule adsorption, these numbers also indicate the number of empty sites on a single SWNT. Green arrows represent possible birth transitions between states with a birth rate of $(N - i)\lambda$ for a population size of i, and red arrows represent possible death transitions between states with a death rate of $i\mu$ for the same population size.

limitation of this method is that it requires sufficient transitions between two adjacent intensity states to obtain an accurate transition matrix. As a consequence, HMM usually requires a relatively large number of transitions to provide accurate parameter estimates. For example, in Figure 6d-iii,iv, we observe that only one transition occurs between two adjacent states during our observation time of 600s, and computing a transition probability matrix through each trace would be insufficient. For the same reason, over 100 traces were needed per film in order to narrow the standard deviation in estimating the rate constant shown in our previous work.[48] Our interest in using these arrays as nanoscale sensors motivates the development of analysis methods that use as few resulting traces as necessary. This will increase both the temporal and spatial resolution.

In order to determine the NO concentration at each SWNT, we adapt a new stochastic analysis method based on an alternative Markov model, the *birth-and-death* process, which we show leads to better accuracy in determining k'_a and k_d. In a birth-and-death Markov model, a population, X_t, undergoes diminutions and additions over a period of observation, t, similar to the fluorescence modulation observed for each nanotube in our experiments. Again, suppose that a single SWNT can be divided into N segments, each of which is the size of the exciton-diffusion length. The fast moving excitons in a single segment can be completely quenched once a single NO molecule adsorbs anywhere on that segment. Therefore, a single SWNT can be simply visualized as a 1D array that contains N reactive sites. In the view of the birth-and-death Markov process, a single SWNT is a population with a maximum population size of N. The exact length of exciton-diffusion does not affect the analysis. An adsorption event results in a fluorescence decrease (quenching) and reduces the unoccupied site population by one. A desorption event therefore is the reverse. How the population size changes over time is of interest, because it directly relates to the observed fluorescence response in time. It is clear that the population size at the next time interval $(t + h)$ is affected by the current population size, X_t, as well as the probability of adsorption or desorption occurring on any individual in the population. Similarly, the number of empty sites on a single SWNT in the next moment is dependent upon the current number of empty sites on the SWNT combined with the single-site adsorption and desorption rates. This process can be described using a typical state transition-rate diagram as shown in Figure 7, or alternatively in a probability form (eq 4), either of which is another representation of the mass action eq 2.

$$P(X_{t+h} = j | X_t = i) =$$

$$\begin{cases} (N - i)k_d h + o(h) & (j = i + 1), \\ 1 - (N - i)k_d h - ik'_a h + o(h) & (j = i), \\ ik'_a h + o(h) & (j = i - 1), \\ o(h) & (\text{otherwise}). \end{cases} \quad (4)$$

More specifically, the probability of a desorption event (the number of empty sites changes from i to $i + 1$) occurring in the next small time interval is proportional $(N - i)k_d$, and the probability of an adsorption event (the number of empty sites changes from i to $i - 1$) is proportional to ik'_a. Note that k'_a is proportional to the concentration of quencher, while k_a, which reflects the very nature of the interaction between NO molecule and SWNT, is a constant. Therefore, an accurate estimation of k'_a provides a proper calibration of the concentration of the quencher. This process mentioned above is not a typical linear birth-and-death process that is well described in literature where both k'_a and k_d are proportional to population size, i. However, applying the theory of the maximum likelihood estimation (MLE)[104,105] to this process allows one to estimate the only two process parameters k'_a and k_d from the observation on the change of site population in a single SWNT. Detailed derivation of the maximum likelihood estimator is available in the Supporting Information. The MLE estimator of these two parameters is given by a two-dimensional vector as below

$$\vec{\theta}_{max} = (\hat{k}'_{a,M}, \hat{k}_{d,M}) = \left(\frac{D_t}{S_t}, \frac{B_t}{N \cdot t - S_t} \right) \quad (5)$$

where D_t and B_t are the number of deaths (adsorption) and births (desorption) in the time interval $[0, t]$, respectively. We use $\hat{k}'_{a,M}$ and $\hat{k}_{d,M}$ to denote MLE estimator for k'_a and k_d. And $B_t + D_t$ equals the total number of transition events. The parameter S_t is defined as $\int_0^t X_u du$, which evaluates the total time lived by the population in the time interval $[0, t]$.

The birth-and-death model employed in this work was derived from the differential eq 2; therefore, it correctly reflects the chemistry of the underlying process; whereas the HMM is just an approximation relying on several nonphysical assumptions. In addition, the time that the underlying process stays at each particular state before the subsequent transition is a random variable whose distribution is obviously state-dependent. While being neglected by HMM, this dependency is explicitly captured by the birth-and-death process.

3.5. Validation of the Stochastic Analysis on Kinetic Monte Carlo (KMC) Simulation. The robustness of the stochastic analysis was tested through applying the birth-and-death MLE method to KMC simulated time-traces using various sets of input rates (denoted as $k'_{a,i}$ and $k_{d,i}$) and different N values. An example simulates 100 traces at four different values of $k'_{a,i}$ (0.0001, 0.001, 0.01, and 0.1 s^{-1}) but the same $k_{d,i}$ of 0.00001 s^{-1}, with $N = 10$ and an observation time of 600 s. These parameters were chosen such that the simulation produces traces that behave similarly to experimental observations in Figure 6d, in order to provide guidance for the accuracy of this stochastic analysis method in our experimental operating condition. As expected, even for the same input rates and N, generated time-traces exhibit different degrees or rates of quenching due to the stochastic nature of the process (Figure 8a), resulting in a distribution of $\hat{k}'_{a,M}$ evaluated from each trace. The histogram of $\hat{k}'_{a,M}$, evaluated using

(104) Keiding, N. *Ann. Stat.* **1975**, *3*, 363.
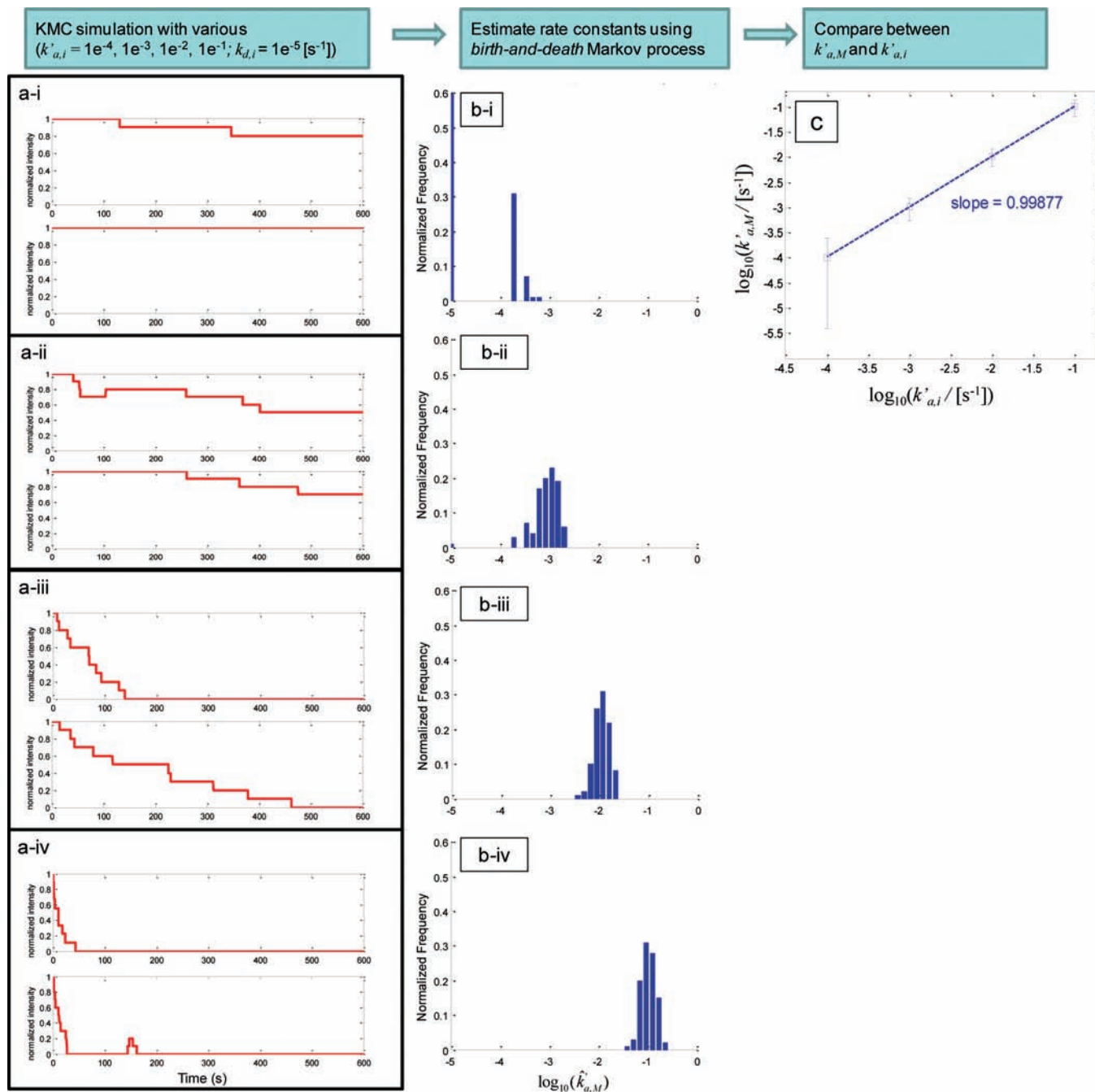(105) Feigin, P. D. *Adv. Appl. Probability* **1976**, *8*, 712.

Figure 8. Kinetic Monte Carlo (KMC) simulation of stochastic quenching on a single SWNT, and the rate constant estimation obtained using the MLE of the birth-and-death Markov process. (a) Representative KMC simulated traces with inputted adsorption rate constants ($k'_{a,i}$) of 0.0001 (a-i), 0.001 (a-ii), 0.01 (a-iii) and 0.1 (a-iv) s^{-1}, and a desorption rate constant ($k_{d,i}$) of 0.00001 s^{-1}. The maximum number of states, N, used in the simulation is 10. Both simulation time and observation time are 600 s. (b) Histogram of $\hat{k}'_{a,M}$ in a $\log_{10}$ scale corresponding to the four simulated conditions in (a). Rate constants smaller than 0.00001 s^{-1} are included in the bin whose rate constant is 0.00001 s^{-1} for better visualization. Each histogram is generated from 100 traces. $\hat{k}'_{a,M}$ of multiple traces is a S_t-weighted average of $\hat{k}'_{a,M}$ from single traces. (c) The $\hat{k}'_{a,M}$ value, evaluated from 100 traces, as a function of $k'_{a,i}$ (square, S_t-weighted average of $\hat{k}'_{a,M}$; error bar, standard deviation of $\hat{k}'_{a,M}$ from each trace). Linear fitting yields a slope of 1, indicating a good agreement between the MLE estimated rates and the input rates.

100 traces each with a 600 s observation time, is centered about $k'_{a,i}$ in each case (Figure 8b). For estimating $\hat{k}'_{a,M}$ from multiple traces, a S_t-weighted average of $\hat{k}'_{a,M}$ is required (Supporting Information). Plotting $\hat{k}'_{a,M}$ against $k'_{a,i}$ yields a slope of unity, proving that $\hat{k}'_{a,M}$ can indeed be used to calibrate $k'_{a,i}$ (Figure 8c). Even 10 traces with an observation time of 600 s can well recover the true $k'_{a,i}$ with a less than 5% deviation (Table 1). A more generalized comparison of $\hat{k}'_{a,M}$, evaluated using various

N, numbers of traces and observation times, are summarized in Table 1, Table S1 and Figure S10, S11, Supporting Information.

While the parity between the obtained $\hat{k}'_{a,M}$ and $k'_{a,i}$ reveals the accuracy of this MLE method, the standard deviation of the distribution (or the width of the histogram) reflects the stochastic nature of the process, whereby for the same set of inputs, each simulated trace always exhibits a slightly different quenching rate. Similarly, in an actual experiment where a small

Table 1. Effect of Observation Time and Number of Traces on $\hat{k}'_{a,M}$ Estimation

$k'_{a,i}$ [s⁻¹][a]	10 traces			100 traces			1000 traces			10,000 traces		
	600 s	3000 s	30000 s	600 s	3000 s	30000 s	600 s	3000 s	30000 s	600 s	3000 s	30000 s
	$\hat{k}'_{a,M}$ [s⁻¹][b]											
1.000×10^{-1}	9.85×10^{-2}	9.84×10^{-2}	9.78×10^{-2}	1.02×10^{-1}	9.94×10^{-2}	1.01×10^{-1}	1.00×10^{-1}	1.01×10^{-1}	9.90×10^{-2}	1.00×10^{-1}	1.00×10^{-1}	1.00×10^{-1}
1.000×10^{-2}	1.05×10^{-2}	1.05×10^{-2}	9.82×10^{-3}	1.05×10^{-2}	9.76×10^{-3}	1.03×10^{-2}	1.01×10^{-2}	9.95×10^{-3}	1.01×10^{-2}	9.98×10^{-3}	1.00×10^{-2}	1.00×10^{-2}
1.000×10^{-3}	9.78×10^{-4}	9.49×10^{-4}	1.02×10^{-3}	1.04×10^{-3}	1.01×10^{-3}	1.03×10^{-3}	1.00×10^{-3}	9.96×10^{-4}	9.93×10^{-4}	1.00×10^{-3}	1.00×10^{-3}	1.00×10^{-3}
1.000×10^{-4}	1.03×10^{-4}	1.03×10^{-4}	9.48×10^{-5}	1.03×10^{-4}	9.64×10^{-5}	1.00×10^{-4}	1.04×10^{-4}	1.01×10^{-4}	9.80×10^{-4}	9.85×10^{-5}	1.01×10^{-4}	9.97×10^{-5}
	$\sigma(\hat{k}'_{a,M})$ [s⁻¹][c]											
1.000×10^{-1}	4.70×10^{-2}	3.60×10^{-2}	3.81×10^{-2}	3.72×10^{-2}	3.56×10^{-2}	1.77×10^{-2}	3.88×10^{-2}	3.71×10^{-2}	3.70×10^{-2}	3.87×10^{-2}	3.83×10^{-2}	3.29×10^{-2}
1.000×10^{-2}	4.49×10^{-3}	3.85×10^{-3}	2.52×10^{-3}	3.78×10^{-3}	3.68×10^{-3}	3.37×10^{-3}	4.08×10^{-3}	3.49×10^{-3}	3.51×10^{-3}	3.85×10^{-3}	3.90×10^{-3}	3.38×10^{-3}
1.000×10^{-3}	3.06×10^{-4}	1.69×10^{-4}	2.38×10^{-4}	4.92×10^{-4}	3.45×10^{-4}	3.63×10^{-4}	5.71×10^{-4}	3.92×10^{-4}	3.40×10^{-4}	5.22×10^{-4}	3.91×10^{-4}	3.39×10^{-4}
1.000×10^{-4}	1.30×10^{-4}	5.18×10^{-5}	2.88×10^{-5}	1.48×10^{-4}	5.75×10^{-5}	4.34×10^{-5}	1.43×10^{-4}	6.74×10^{-5}	3.68×10^{-5}	1.37×10^{-4}	6.76×10^{-5}	3.60×10^{-5}
	% error = $(\hat{k}'_{a,M} - k'_{a,i})/k'_{a,i} \times 100\%$											
1.000×10^{-1}	−1.46	−1.58	−2.25	2.03	−0.56	1.39	0.25	1.11	−0.99	0.28	0.29	0.01
1.000×10^{-2}	4.57	5.16	−1.76	4.71	−2.41	2.67	0.68	−0.51	0.63	−0.24	0.47	0.33
1.000×10^{-3}	−2.17	−5.12	2.02	3.69	1.07	3.34	0.30	−0.44	−0.67	0.29	0.19	0.09
1.000×10^{-4}	3.08	3.45	−5.21	3.30	−3.58	0.15	3.52	1.30	−2.00	−1.48	0.88	−0.29

[a] Four sets of input adsorption rates, $k'_{a,i}$, for KMC simulated traces. [b] S_r-weighted average $\hat{k}'_{a,M}$. [c] S_r-weighted standard deviation of $\hat{k}'_{a,M}$. Simulation is performed at $k'_{d,i} = 0.00001$ s⁻¹ and $N = 10$.

number of quenching molecules is added, each sensor produces slightly different time-traces due to the probability distribution of the quencher molecule adsorbed on each sensor, and we will also expect a distribution of the sensor responses. The standard deviation of the distribution decreases as the observation time increases, which eventually approaches a lower limit that is due solely to stochasticism. Large sets of simulation results suggest that the number of traces does not affect the standard deviation of the distribution, and this lower limit is always about 30% of $k'_{a,i}$ (Table 1). The speed in which the standard deviation of the distribution converges to its limiting value is input rate-dependent. It turns out that for high $k'_{a,i}$ (0.1 s⁻¹, 0.01 s⁻¹), the standard deviation easily reaches its lower bound even using 600 s observation of 10 traces; however, for low $k'_{a,i}$ (0.0001 s⁻¹) to reach this lower bound, it requires an increase of observation time (Table 1). This is because at low $k'_{a,i}$, very few transitions occur within the first 600 s. Recording sufficient transitions within longer observation time will allow us to obtain a more accurate $\hat{k}'_{a,M}$ for each trace, resulting in a distribution of $\hat{k}'_{a,M}$ solely due to the stochastic nature. However, it is worth noting even when there may not be sufficient transitions in a single trace, the $\hat{k}'_{a,M}$ from just 10 traces is still very accurate (within 5% error from the true value of $k'_{a,i}$). This again shows the advantage of the MLE model whereby only two parameters require estimation, $\hat{k}'_a$ and k_d, and therefore not many transitions are needed to provide an accurate parameter evaluation.

3.6. Calibration of the Sensor Platform by Exposing the SWNT Array to Aqueous NO Solution. Determination of the NO Adsorption Rate Constant. Calibration of the AT_{15}−SWNT sensor array was carried out by exposing the array to aqueous NO solution at different concentrations, ranging from 0.16 μM to 19.4 μM (Figure 6). A custom-written MATLAB program automatically selects the 50 brightest diffraction-limited spots with each representing a single SWNT and extracts the fluorescence intensity in time, resulting in a set of 50 time-traces for each experiment. We chose the brightest SWNTs to ensure they have fewer defects chemically and structurally[56−58] and therefore are most sensitive to the changes in the environment. Each time-trace is then subjected to another custom-written MATLAB routine based on a chi-squared error-minimizing step-finding algorithm described in ref 106 to distinguish real transition events from noise (Figure 6d, black). The program results in the same fitting steps compared to HMM-based step-finding algorithm[48,49,103] but reduces the computational time by 90%.[107]

Once all the transitions are identified, we apply the birth-and-death MLE to each time-trace, and each SWNT reports a $\hat{k}'_{a,M}$. At these low concentrations (∼0.2−20 μM), each sensor detects a slightly different concentration of NO, mainly due to

(106) Kerssemakers, J. W. J.; Laura Munteanu, E.; Laan, L.; Noetzel, T. L.; Janson, M. E.; Dogterom, M. *Nature* **2006**, *442*, 709.

(107) Both algorithms fail when applied to control data in which there are no actual transitions, fitting steps within the noise (Figure S12, Supporting Information). We attempted to subject each trace to a noise reduction program based on ref 108 before applying HMM or error-minimizing step-finding algorithms, but the overfitting of noise on control data persisted (Figure S12). We therefore concluded that these algorithms cannot be utilized on traces containing no authentic transitions. To resolve this issue, we first determine which traces contain actual transitions in fluorescence intensity and perform the analysis only on these data sets. The relatively high signal-to-noise ratio in the data aids in this, and bias is minimized through randomizing all traces prior to analysis (Figure S12). And the step-fitting algorithm is applied thereafter only to traces that contain transitions, and zero-transitions are assigned to the remainder.

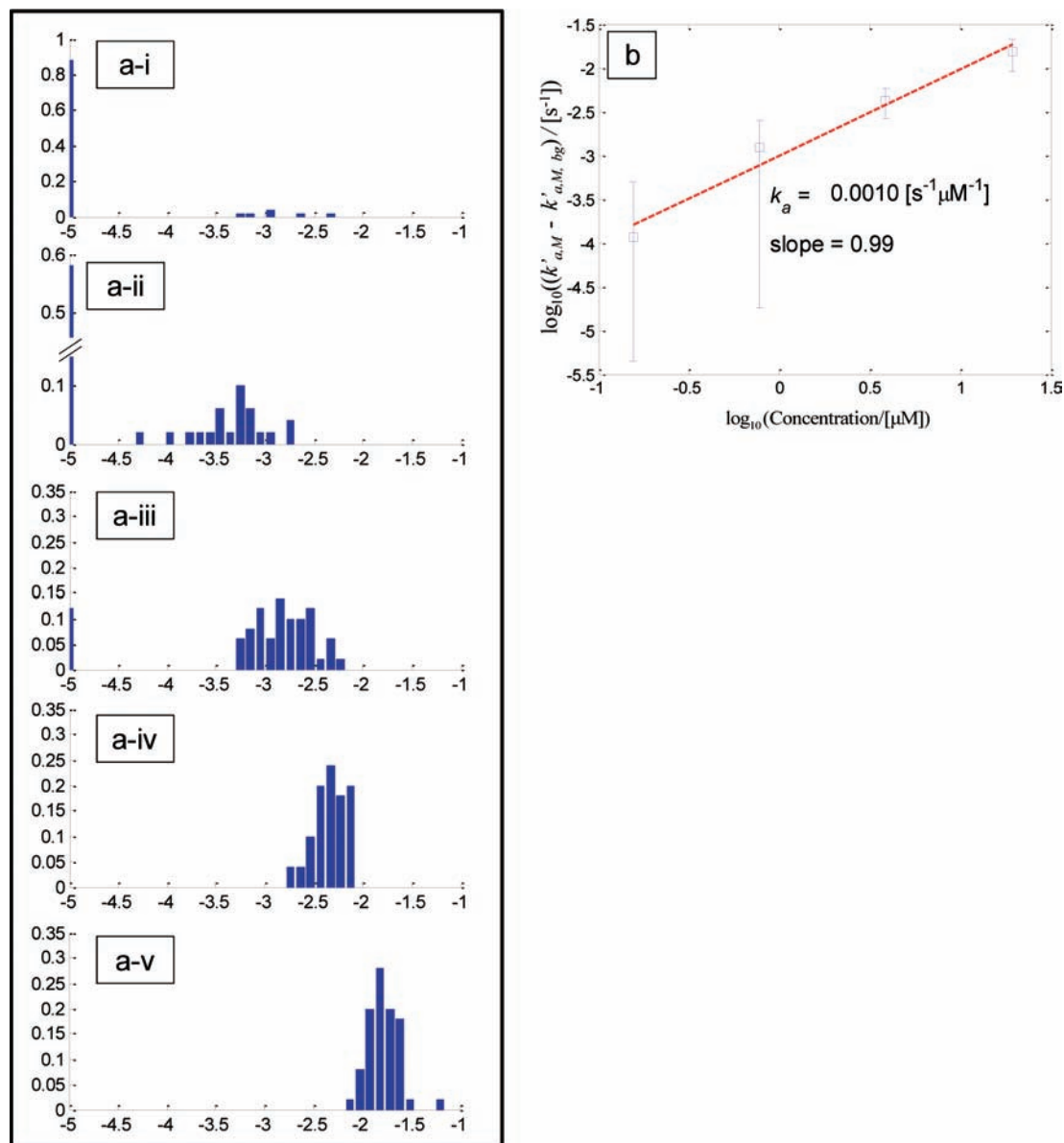(108) Chung, S. H.; Kennedy, R. A. *J. Neurosci. Methods* **1991**, *40*, 71.

Figure 9. Calibration of the AT$_{15}$–SWNT sensor array with NO solution. (a) Cumulative histogram of $\hat{k}'_{a,M}$ values obtained from each SWNT in the array upon exposure to NO at five different concentrations (a-i, 0 μM; a-ii, 0.16 μM; a-iii, 0.78 μM; a-iv, 3.9 μM; a-v, 19.4 μM). Rate constants lower than 0.00001 s^{-1} are grouped into the smallest bin. (b) The effective $\hat{k}'_{a,M}$, or ($\hat{k}'_{a,M} - \hat{k}'_{a,M,bg}$), evaluated from 50 time-traces, as a function of NO concentration (square, S_t-weighted average of $\hat{k}'_{a,M}$; error bar, S_t-weighted standard deviation of $\hat{k}'_{a,i}$ from each trace). The data is plotted on a log$_{10}$-log$_{10}$ scale for better visualization of low concentration data. Fitting the data yields a slope of 1 (red dotted line), agreeing with eq 3, $k'_a = k_a[NO]$, with k_a of 0.001 s^{-1} μM NO^{-1}.

the stochastic nature of the process, which results in a distribution of the $\hat{k}'_{a,M}$ that increases as the NO concentration increases (Figure 9a). Close examination yields that 8 out of 50 sensors in the control experiment, in which no NO is added, also exhibit a limited number of transitions, which may be attributed to the proton adsorption on the SWNT. MLE analysis of the control experiment yields a rate describing the background fluctuation, or $\hat{k}'_{a,M,bg}$, of 0.0001 s^{-1}. After subtracting this contribution from the $\hat{k}'_{a,M}$ values obtained at other concentrations, the observed rate constant is linearly dependent on the NO concentration with a slope of 1 (Figure 9b), agreeing with eq 3. The y-intercept of the fitted line reports a k_a of 0.001 s^{-1} μM NO^{-1}, which provides a good calibration of the sensor array. Considering the diffusive and highly reactive property of NO, the linear trend observed experimentally is noteworthy. We estimate the ensemble detection limit as 300 nM, or 3 times the ratio of $\hat{k}'_{a,M,bg}/k_a$, since the background fluctuations are limiting. However, the sensor is

infinitely photostable and does not intrinsically blink, allowing immobilization of large arrays. These large arrays can act as sensors that are independently addressable, as we have shown previously for H$_2$O$_2$.[49] One advantage of such an array is that NO generation can be tracked spatially, although this is still constrained by optical diffraction limit. In addition, while the standard deviation evaluated at a relatively high concentration (3.9 and 19.4 μM) lies within the lower limit estimated through KMC, the standard deviations are higher than expected when the NO concentration further decreases. This might be because the inhomogeneity of the SWNT starts to play a role when the concentration of the analytes becomes low, since sensors possessing more defect sites are less sensitive to small changes and do not respond at low NO local concentration.

We note that single stochastic sensors of this type do not have a conventional detection limit that may be compared with an ensemble measurement. If placed near a nanometer scale

generator of NO, such as a living macrophage or immobilized NO synthase, this platform can easily detect the product. The resulting bulk concentration may be trace, but such a nanometer scale sensor may potentially be used to map the concentration profile in and around the generator. We have demonstrated this for the case of a H_2O_2 selective array and studied the H_2O_2 signaling from protein EGFR as a local generator.[48,49] Future work will extend this approach to living systems involving NO.

4. Conclusions

The selective detection of single nitric oxide molecules using a specific DNA sequence d(AT)$_{15}$, adsorbed to single-walled carbon nanotubes (AT$_{15}$−SWNT) is reported. This sequence is distinct from eight other DNA variants that show fluorescence quenching or enhancement from a library of tested analytes including dopamine, NADH, L-ascorbic acid, and riboflavin. The d(AT)$_{15}$ imparts SWNTs with a distinct selectivity toward NO. Polyvinyl alcohol-wrapped SWNTs show no response to NO but exhibit enhancement responses to other molecules in the tested library. The wrapping molecules have shown to significantly affect the selectivity of the SWNT complex. A NO sensing platform is developed, consisting of an array of individually deposited AT$_{15}$−SWNT. A stepwise fluorescence decrease is observed when the sensor is exposed to NO, reporting single-molecule NO adsorption via SWNT exciton quenching. We describe these quenching traces using a birth-and-death Markov model, whose maximum likelihood estimator reports the adsorption and desorption rates of NO. Applying the method to KMC simulated traces suggests a less than 5% deviation in estimation under our experimental conditions, allowing for calibration using a series of NO concentrations. The adsorption rate shows a linear dependence upon NO concentration, and the intrinsic single-site NO adsorption rate constant is 0.001 s^{-1} μM NO^{-1}. The ability to detect NO quantitatively at the single molecule level has applications for the study of NO carcinogenesis, chemical signaling, and medical diagnostics for inflammation.

Supporting Information Available: Additional experimental data are available, including AFM images, SWNT absorption spectra, and single-molecule fluorescence response time-traces. Detailed discussions on KMC and MLE methods, and Hyper-Chem simulations are also provided. A movie file showing the intensity modulation of a diffraction-limited spot on the sensor array upon exposure to 3.9 μ M NO is also available. This information is available free of charge via the Internet at http://pubs.acs.org/.

JA1084942